J. Fluid Mech. (1993), *vol.* 253, *pp.* 327–340

A fast kinematic dynamo in two-dimensional time-dependent flows

By NIELS F. OTANI
School of Electrical Engineering, Cornell University, Ithaca, NY 14853, USA

(Received 10 November 1992 and in revised form 10 February 1993)

A time-continuous, constant-resistivity version of the fast dynamo model introduced by Bayly & Childress (1988) is studied numerically. The expected dynamo mechanism in this context is described and is shown to be operative in the simulations. Exponential growth of the fastest growing mode is observed, with the growth rate for the smallest resistivity attempted ($1/R_m = 10^{-4}$) agreeing well with the Bayly–Childress model. It is argued, based on the long- and short-wavelength behaviour of the mode for different resistivities, that the growth rates obtained for the $R_m = 10^4$ case should persist as $R_m \rightarrow \infty$.

1. Introduction

An understanding of how and when magnetic fields can be generated from the flow of an electrically conducting fluid is important to our understanding of many problems including the generation of the Earth's, the Sun's, and others stars' magnetic fields and the formation of coronas around the Sun and other stars. Specifically related to the magnetic field structures of the Sun is the problem of how such fields can be produced in the limit of infinite electrical conductivity. Magnetic Reynolds numbers R_m of 10^{10} or higher are typical of the Sun and its corona. Magnetic field generation under these circumstances ($R_m \rightarrow \infty$) is usually referred to as a fast dynamo process (Vaĭnshteĭn & Zel'dovich 1972) and has been of considerable interest in the past few years. The existence of fast dynamos is important not only to such problems, but is also of interest in its own right, representing a fundamental characteristic of the relationship between magnetic fields and matter.

Several types of flows which could lead to fast dynamo action have been suggested, as reviewed recently in Childress *et al.* (1990) and Roberts & Soward (1992). Among these are steady two- and three-dimensional flows (Soward 1987) including the 'ABC' class of flows (Arnol'd & Korkina 1983; Dombre *et al.* 1986; Galloway & Frisch 1986; Gilbert & Childress 1990; Gilbert 1991), chaotic flows resulting from overlapping resonances (Strauss 1986), flows associated with coordinate mappings (Bayly & Childress 1987, 1988; Finn & Ott 1988), and unsteady two-dimensional flows (Galloway & Proctor 1992). The flows employed in the study presented here fall in this last category, with early results originally reported in Otani (1988).

In this paper, two computer codes are used to examine the possibility of the presence of a fast dynamo in a prescribed flow (the 'kinematic' fast dynamo problem). Two flows are considered for this study: the first is a time-continuous version of the flow examined by Bayly & Childress (1987, 1988, 1989), while the second is a closely related variant. An advantage of the Bayly–Childress flow is that neither the flow itself nor its vorticity contains singularities. The flow thus has physically realizable analogues, the flow used in this study being one example. The aim of this research is to determine if the positive results obtained by Bayly & Childress with respect to the presence of a fast dynamo apply to the actual flow situation corresponding to the mapping they use in their work.

2. The equations

The evolution of the magnetic field $\boldsymbol{B}$ in the magnetohydrodynamic (MHD) dynamo problem is governed by

$$\frac{\partial \boldsymbol{B}}{\partial t} = \nabla \times (\boldsymbol{u} \times \boldsymbol{B}) + \eta \nabla^2 \boldsymbol{B}, \tag{1}$$

which is derived from Faraday's law, Ampère's law without displacement current, and Ohm's law. When $\nabla \cdot \boldsymbol{u} = 0$, as it always is for the work presented here, (1) is equivalent to

$$\frac{\partial \boldsymbol{B}}{\partial t} = -\boldsymbol{u} \cdot \nabla \boldsymbol{B} + \boldsymbol{B} \cdot \nabla \boldsymbol{u} + \eta \nabla^2 \boldsymbol{B}. \tag{2}$$

In these equations, η is a constant electrical resistivity and $\boldsymbol{u}$ is a specified, two-dimensional, time-dependent, incompressible, spatially periodic flow. We use two very similar flows in this work,

$$\boldsymbol{u}(x, y, t) = 2(\hat{y}\beta \sin x + \hat{z}\alpha \cos x)\cos^2 \omega_0 t + 2(\hat{x}\beta \sin y + \hat{z}\alpha \cos y)\sin^2 \omega_0 t \tag{3}$$

and

$$\boldsymbol{u}(x, y, t) = 2(\hat{y}\beta \sin x + \hat{z}\alpha \cos x)\cos^2 \omega_0 t + 2(-\hat{x}\beta \sin y + \hat{z}\alpha \cos y)\sin^2 \omega_0 t, \tag{4}$$

with α, β, and ω_0 being constant parameters. The system is periodic in each of the orthogonal directions $\hat{x}$, $\hat{y}$, and $\hat{z}$, with periodicity length 2π in the $\hat{x}$- and $\hat{y}$-directions, and $2\pi/k_z$ in the $\hat{z}$-direction. The system is initialized with a seed field of the form $\boldsymbol{B}(\boldsymbol{x}, t=0) = \hat{x}B_0 \exp(\mathrm{i}k_z z)$, where B_0 and k_z are constants.

The flow described by (3) is essentially identical to the one proposed by Bayly & Childress, except that the square-wave 'pulses' in the flow have been smoothed so as to be continuous in time, varying as $\sin^2 \omega_0 t$ and $\cos^2 \omega_0 t$. Additionally, the system itself is essentially the same as the Bayly–Childress model, except that the electrical resistivity η is not turned on and off, but is instead held constant throughout the simulation. The Bayly–Childress model is thus recast into a more realistic, physically realizable form.

The dynamo action expected of this flow is of the stretch–fold–shear variety (cf. the mapping discussed in Bayly & Childress 1988). Figure 1 illustrates the mechanism. Assume that, initially, the $\hat{x}$-component of the magnetic field is non-zero when averaged over x and y. We take this mean field as the seed magnetic field for the dynamo action we outline here. (The term 'mean' magnetic field in this paper refers to the x- and y-averaged magnetic field at a given z; the overall z-averaged magnetic field is always zero in all the models we employ.) The field is initially and always defined to be the real part of a function having a dependence in the z-direction of $\exp(\mathrm{i}k_z z)$; thus, on constant-z planes separated by π/k_z, the field will point in opposite directions, as shown in figure 1(*a*).

The $\hat{y}$-component of the $\cos^2 \omega_0 t$ term in the flow given by (3) can be represented in simplified form on each of these planes by the arrows shown in figure 1(*b*). This component of the flow will tend to stretch the field, yielding the configuration depicted in figure 1(*c*). The essential feature of this field is the spatial arrangement of its $\hat{y}$-component, displayed in figure 1(*d*). The strength of this generated $\hat{y}$ magnetic field is determined by the flow parameter β.

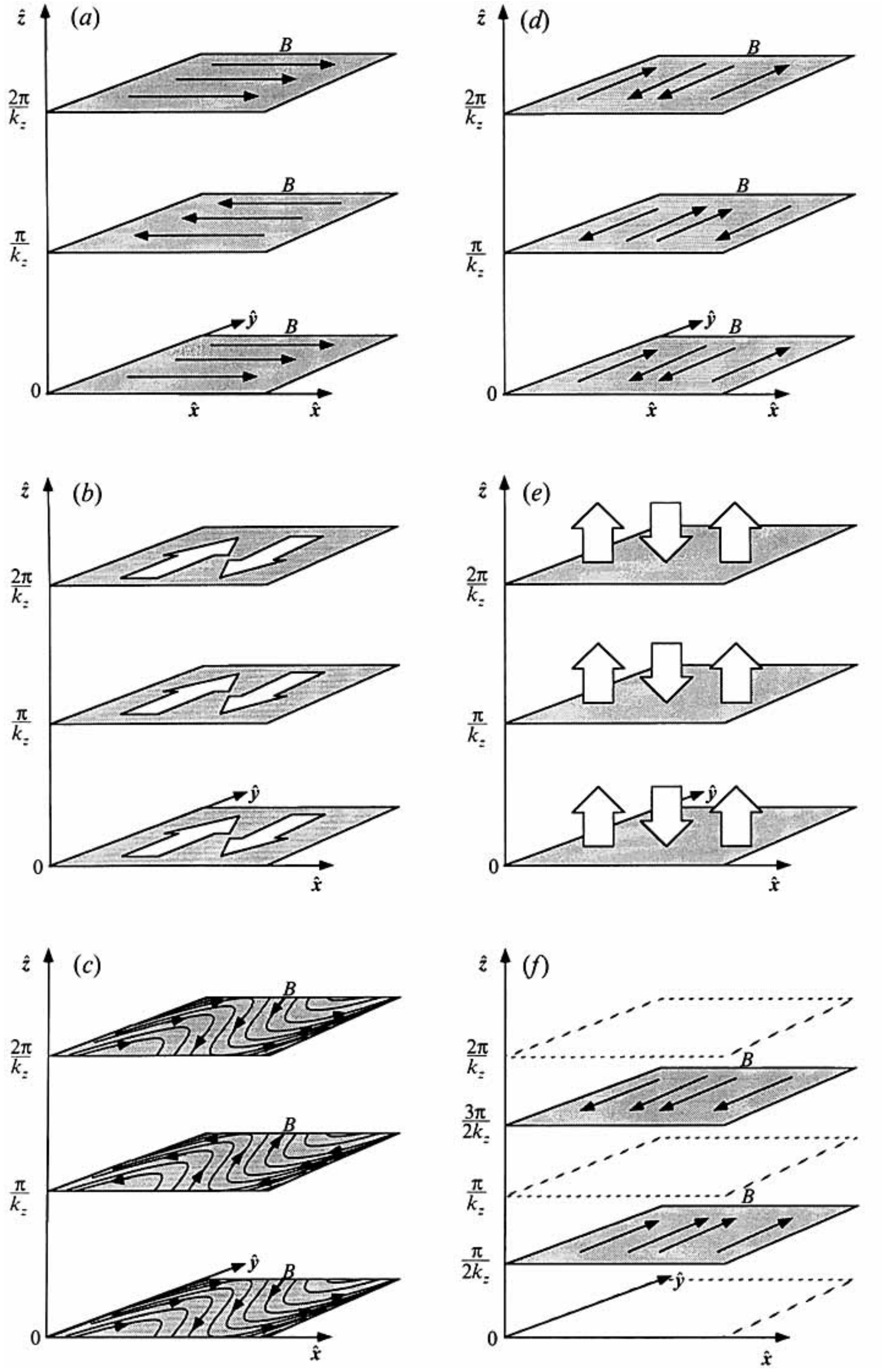

FIGURE 1. Illustration of a simplified model of the dynamo action expected to be present for the flows employed in this study. (*a*) Orientation of the seed magnetic field B_x on three constant-z planes. (*b*) Sketch of the $\hat{y}$-component of the flow pulse. (*c*) Effect of the $\hat{y}$-component of the flow on the seed magnetic field. (*d*) Essential arrangement of the $\hat{y}$-component of the magnetic field illustrated in (*c*). (*e*) Sketch of the $\hat{z}$-component of the flow pulse. (*f*) Effect of the $\hat{z}$-component of the flow on the magnetic field shown in (*d*).

The $\hat{z}$-component of the $\cos^2 \omega_0 t$ term in (3), shown in figure 1 (*e*), acts simultaneously with the $\hat{y}$-component to push the $\hat{y}$-component of the magnetic field up and down between the planes illustrated. If the parameter α is adjusted appropriately ($\alpha \sim 0.5$ for $k_z = 1$ and $\omega_0 = 1$), the effect of the $\hat{z}$-directed flow will be to push similarly directed $\hat{y}$-components of the magnetic field into constant-z planes positioned halfway between the original planes (figure 1 *f*). This new mean field B_y can easily be made larger than the original seed field B_x by, for example, adjusting β, thereby producing a positive dynamo effect. The conjecture of Finn *et al.* (1991) is relevant here, suggesting that the dynamo effect should persist in the $R_m \rightarrow \infty$ limit. Once the mean field B_y is created, the situation is again essentially the same as figure 1 (*a*), with the new field ready to serve as the seed field for the next flow pulse (the $\sin^2 \omega_0 t$ term).

It is this next pulse which distinguishes (3) and (4). When the $\cos^2 \omega_0 t$ flow in (4) is rotated 90° so that $\hat{x} \rightarrow \hat{y}$ and $\hat{y} \rightarrow -\hat{x}$, the result is the $\sin^2 \omega_0 t$ flow. It follows that the helicities of both flow pulses are the same, so we refer to cases involving flows of the form defined by (4) as *non-reversing helicity* cases. Since the B_y seed field on which the $\sin^2 \omega_0 t$ flow operates is, apart from an inconsequential translation in $\hat{z}$, similarly rotated from the B_x seed field, the actions of both pulse terms in (4) on their corresponding seed fields are identical (within this simplified model). Note also that the result of the action of the $\sin^2 \omega_0 t$ pulse is to generate a mean B_x field in the same direction as the original B_x seed field on which the $\cos^2 \omega_0 t$ pulse previously acted.

In contrast, the $\sin^2 \omega_0 t$ term of the Bayly–Childress-equivalent flow, (3), is a mirror image ($\hat{x} \rightarrow -\hat{x}$) of the $\sin^2 \omega_0 t$ term in (4). We thus refer to cases involving flows defined by (3) as *reversing helicity* cases. The B_x field generated by the $\sin^2 \omega_0 t$ pulse is antiparallel to the field that existed before the application of the $\cos^2 \omega_0 t$ flow pulse.

This simplified description of the dynamo action in our model can provide the basis for an estimate of the magnetic field growth. Consider the effect of a single pulse flow of the form

$$\boldsymbol{u}(x, t) = 2(\beta \hat{y} \sin x + \alpha \hat{z} \cos x) \sin^2 \omega_0 t \quad \text{for} \quad 0 \leqslant t \leqslant \pi/\omega_0 \tag{5}$$

on a seed field $\boldsymbol{B}(t=0) \equiv (B_{x0}, 0, 0)\, \mathrm{e}^{\mathrm{i}k_z z}$. Neglecting diffusion, (2) yields

$$\frac{\partial B_x}{\partial t} = -u_z \frac{\partial B_x}{\partial z}, \tag{6a}$$

$$\frac{\partial B_y}{\partial t} = -u_z \frac{\partial B_y}{\partial z} + B_x \frac{\partial u_y}{\partial x}. \tag{6b}$$

The second term on the right-hand side of (6*b*) generates the $\hat{y}$-component of the magnetic field in figures 1 (*c*) and 1 (*d*) which is then advected in the $\hat{z}$-direction (figure 1 *e*) by the first term. Equation (6*a*) simply yields the advection of B_x by u_z:

$$B_x = B_{x0} \exp\left(-\mathrm{i}k_z \xi_z(t)\, \alpha \cos x\right) \mathrm{e}^{\mathrm{i}k_z z}, \tag{7}$$

where

$$\xi_z(t) \equiv \int_0^t \mathrm{d}t' 2 \sin^2 \omega_0 t' = t - \frac{\sin 2\omega_0 t}{2\omega_0},$$

which, when scaled by α, is just the maximum displacement due to u_z after time t. When (7) is substituted into (6*b*) and the result integrated to $t = \pi/\omega_0$ (one pulse duration) the resulting $\hat{y}$-magnetic field is

$$B_y(t = \pi/\omega_0) = \frac{\pi \beta B_{x0}}{\omega_0} \cos x \exp\left(-\mathrm{i}k_z (\pi/\omega_0)\, \alpha \cos x\right) \mathrm{e}^{\mathrm{i}k_z z}. \tag{8}$$

By averaging over x and y, we obtain an estimate of the growth of the mean magnetic field per flow pulse:

$$\frac{\langle B_y(t=\pi/\omega_0)\rangle_{x,y}}{B_{x0}} = -\mathrm{i}\frac{\pi\beta}{\omega_0}J_1\left(k_z\frac{\pi}{\omega_0}\alpha\right), \tag{9}$$

where J_1 is a first-order ordinary Bessel function.

3. The numerical model

Equations (1) and (2) are most easily solved in terms of the spatial Fourier coefficients of $\boldsymbol{B}$. Use of this type of method (spectral method) is particularly efficient for this flow, because a Fourier mode characterized by wavenumber $\boldsymbol{k} \equiv (k_x, k_y, k_z)$ couples only to itself and the modes $(k_x \pm 1, k_y \pm 1, k_z)$, thus minimizing the number of calculations required per simulation timestep Δt. This also implies that the different values of k_z are independent of one another, and may be studied individually in separate runs. Furthermore, the form of the equations allows both codes to run fully vectorized on Cray machines.

To ensure numerical stability, a predictor–corrector method is used to advance the magnetic fields in time. The resistive term is done implicitly. Specifically, the timestep algorithm used for (2) is

$$\begin{aligned} \boldsymbol{B}_a(\boldsymbol{k}) = \boldsymbol{B}_{\mathrm{old}}(\boldsymbol{k}) + \epsilon\Delta t \sum_{\pm} \{ & -\mathrm{i}[(\boldsymbol{k}\mp\hat{\boldsymbol{x}})\cdot\boldsymbol{u}(\pm\hat{\boldsymbol{x}})]\,\boldsymbol{B}_{\mathrm{old}}(\boldsymbol{k}\mp\hat{\boldsymbol{x}}) \\ & -\mathrm{i}[(\boldsymbol{k}\mp\hat{\boldsymbol{y}})\cdot\boldsymbol{u}(\pm\hat{\boldsymbol{y}})]\,\boldsymbol{B}_{\mathrm{old}}(\boldsymbol{k}\mp\hat{\boldsymbol{y}}) \\ & \pm\mathrm{i}[\hat{\boldsymbol{x}}\cdot\boldsymbol{B}_{\mathrm{old}}(\boldsymbol{k}\mp\hat{\boldsymbol{x}})]\,\boldsymbol{u}(\pm\hat{\boldsymbol{x}}) \\ & \pm\mathrm{i}[\hat{\boldsymbol{y}}\cdot\boldsymbol{B}_{\mathrm{old}}(\boldsymbol{k}\mp\hat{\boldsymbol{y}})]\,\boldsymbol{u}(\pm\hat{\boldsymbol{y}})\}, \end{aligned} \tag{10a}$$

$$\boldsymbol{B}_{\mathrm{pred}}(\boldsymbol{k}) = (1+\eta k^2\epsilon\,\Delta t)^{-1}\boldsymbol{B}_a(\boldsymbol{k}), \tag{10b}$$

$$\begin{aligned} \boldsymbol{B}_b(\boldsymbol{k}) = \boldsymbol{B}_{\mathrm{old}}(\boldsymbol{k}) + \Delta t \sum_{\pm} \{ & -\mathrm{i}[(\boldsymbol{k}\mp\hat{\boldsymbol{x}})\cdot\boldsymbol{u}(\pm\hat{\boldsymbol{x}})]\,\boldsymbol{B}_{\mathrm{pred}}(\boldsymbol{k}\mp\hat{\boldsymbol{x}}) \\ & -\mathrm{i}[(\boldsymbol{k}\mp\hat{\boldsymbol{y}})\cdot\boldsymbol{u}(\pm\hat{\boldsymbol{y}})]\,\boldsymbol{B}_{\mathrm{pred}}(\boldsymbol{k}\mp\hat{\boldsymbol{y}}) \\ & \pm\mathrm{i}[\hat{\boldsymbol{x}}\cdot\boldsymbol{B}_{\mathrm{pred}}(\boldsymbol{k}\mp\hat{\boldsymbol{x}})]\,\boldsymbol{u}(\pm\hat{\boldsymbol{x}}) \\ & \pm\mathrm{i}[\hat{\boldsymbol{y}}\cdot\boldsymbol{B}_{\mathrm{pred}}(\boldsymbol{k}\mp\hat{\boldsymbol{y}})]\,\boldsymbol{u}(\pm\hat{\boldsymbol{y}})\}, \end{aligned} \tag{10c}$$

$$\boldsymbol{B}_{\mathrm{new}}(\boldsymbol{k}) = (1+\eta k^2\Delta t)^{-1}\boldsymbol{B}_b(\boldsymbol{k}), \tag{10d}$$

where $\boldsymbol{B}(\boldsymbol{k})$ and $\boldsymbol{u}(\boldsymbol{k})$ are the Fourier transforms of $\boldsymbol{B}$ and $\boldsymbol{u}$, and $\epsilon > 0.5$ is required for numerical stability. A similar set of equations is used for (1).

We used as our primary simulation code the one modelling (2), because it ran somewhat faster than the code for (1). The code for (1) was run occasionally to verify that both codes were operating properly. When both were run, they agreed to a very high degree of accuracy. We also verified the codes by using them to compute $\nabla\cdot\boldsymbol{B}$. When checked, it was zero to one part in 10^{12}.

Normally, the codes followed all three components of the magnetic field. Note, however, that the computation of B_x and B_y does not depend on B_z. When B_z was not needed for diagnostic purposes or for verifying $\nabla\cdot\boldsymbol{B} = 0$, it was often omitted, allowing the code to run with a 50% increase in speed.

4. Results

The parameters for our runs were chosen so that the simplified dynamo model described above would be relevant. Except where otherwise indicated, the parameters $\alpha = 0.5$, $\beta = 1.0$, $k_z = 1.0$, and $\omega_0 = 1.0$ were used, which, according to the simplified

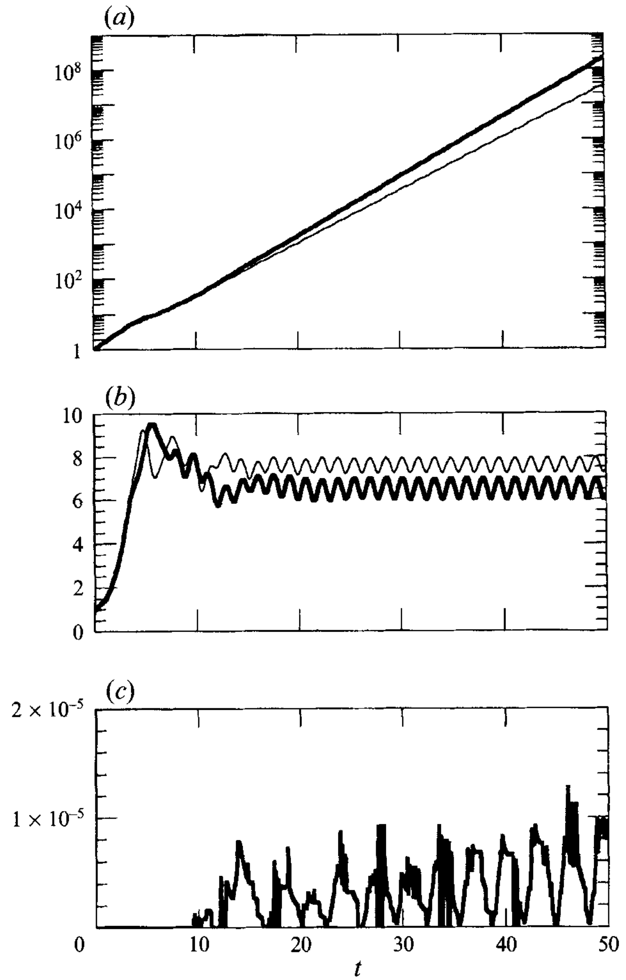

FIGURE 2. Plots *vs*. time of (*a*) $[\Sigma_k|\boldsymbol{B}(\boldsymbol{k})|^2]^{\frac{1}{2}}$ for the cases of reversing and non-reversing helicities; (*b*) $\langle k^2\rangle^{\frac{1}{2}} \equiv [\Sigma_k k^2|\boldsymbol{B}(\boldsymbol{k})|^2/\Sigma_k|\boldsymbol{B}(\boldsymbol{k})|^2]^{\frac{1}{2}}$, for the cases of reversing and non-reversing helicities, and (*c*) $|\mathrm{Re}[B_x(\boldsymbol{k}=0;k_{max}=64)]-\mathrm{Re}[B_x(\boldsymbol{k}=0;k_{max}=32)]|/[\mathrm{Re}[B_x(\boldsymbol{k}=0;k_{max}=64)]^2+\mathrm{Im}[B_y(\boldsymbol{k}=0;k_{max}=64)]^2]^{\frac{1}{2}}$. ━━, reversing helicity; ——, non-reversing helicity.

model, should exhibit dynamo action. With $\eta = 2.513 \times 10^{-3}$, the inverse magnetic Reynolds number, defined here as $R_m^{-1} = \eta T/L^2$, is 10^{-4} for our case, where $T = \pi/2\omega_0$ is the effective pulse length and $L = 2\pi$ is a characteristic system length. The numerical parameters $\Delta t = 0.01$ or 0.005 and $\epsilon = 0.65$ were used in all the simulations discussed here. Wavenumbers in the square region $-32 \leqslant k_x, k_y \leqslant 32$ were kept, with modes with either k_x or k_y equal to ± 33 defined to be 0 at all times t.

Typical time series obtained from our simulations are illustrated in figures 2 and 3. After an initial transient, the magnetic field energy was observed to grow with fairly clear exponential growth for several tens of flow pulses (figure 2*a*). Similarly, our simple measure of the relative participation of the various Fourier modes, the root-mean-square wavenumber, settles down following the initial transient to a steady pattern which oscillates in synchrony with the flow pulses. The steadiness of the pattern indicates that the simulation has been run long enough to include fully the shortest wavelengths followed by the simulation. Figure 2(*c*) suggests that enough wave-

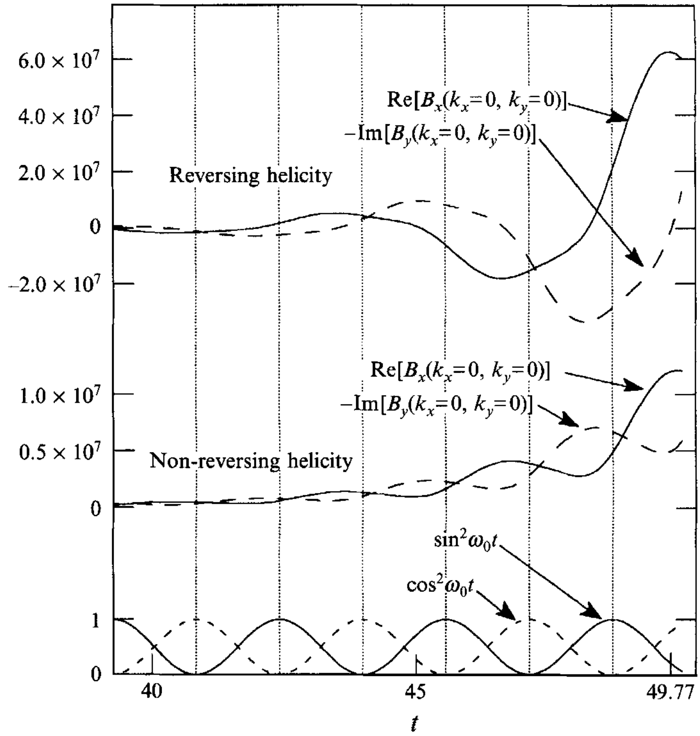

FIGURE 3. Plots *vs.* time of $\mathrm{Re}[B_x(k=0)]$ and $-\mathrm{Im}[B_x(k=0)]$ for the reversing and non-reversing helicity cases. Also shown for reference are the functions $\cos^2\omega_0 t$ and $\sin^2\omega_0 t$. The time designated as $t = 49.77$ indicates the time at which figures 5 and 7(*a*) were made.

numbers were kept – when the same simulation was run with $-64 \leqslant k_x, k_y \leqslant 64$, the relative change in the mean magnetic field was of order 10^{-5}.

The time envelopes of the real and imaginary parts of the mean field components were observed to grow exponentially with the same growth rate as the square root of the magnetic field energy. The components' detailed time dependence, well after the initial transient, is shown in figure 3. The $\mathrm{Re}[B_x(k_x=0, k_y=0)]$ component shown in the figure is equivalent to the mean $\hat{x}$ magnetic field at $z = 0$ (cf. figure 1), while $-\mathrm{Im}[B_y(k_x=0, k_y=0)]$ corresponds to the mean value of B_y at $z = \pi/2k_z$. As predicted by the simplified model, both components of the mean magnetic field alternate sign in the reversing-helicity case, and never change sign in the non-reversing-helicity case. Also as predicted by the model, extrema in the reversing-helicity case and maxima in the non-reversing-helicity case occur for B_x and B_y shortly after the peaks in the $\sin^2\omega_0 t$ and $\cos^2\omega_0 t$ functions, respectively.

A comparison of the growth rates from the simulations with those predicted by theory is shown in figure 4. The simulation growth rates agree quite closely with those found by Bayly & Childress (1988) (trace *b*) for the lowest resistivity examined ($R_m = 10^4$, trace *c*), with growth rates for the higher resistivities (e.g. $R_m = 10^3$, trace *d*) converging on the $R_m = 10^4$ values as the resistivity was decreased. This suggests that the Bayly–Childress mapping model is a good representation in the large-R_m limit of the physically realizable model we employ here. Trace (*e*) in figure 4 is a plot of the growth rates from the simplified dynamo model (equation (9)) *vs.* α. It agrees most closely with the other traces in the vicinity of $\alpha = 0.5$, which corresponds to those values of α which bring similarly directed magnetic fields to the same constant-z plane

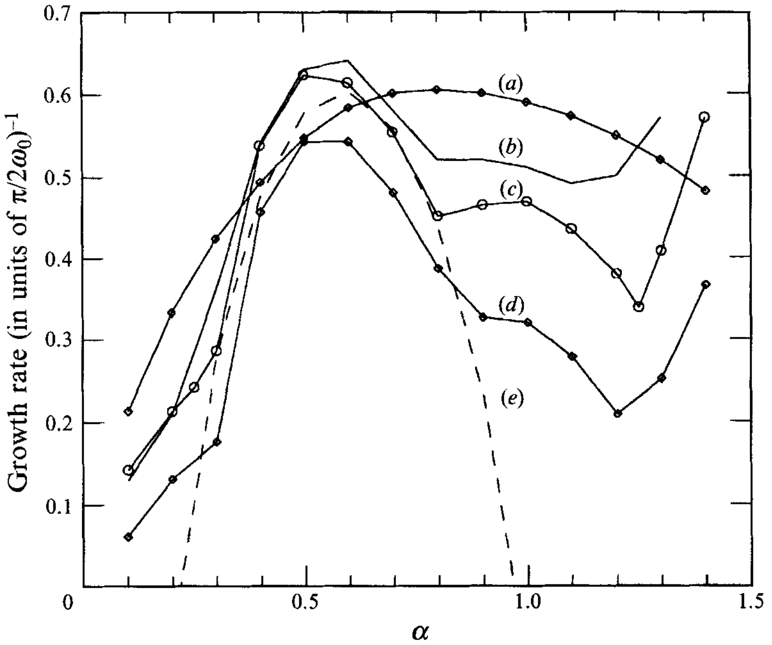

FIGURE 4. Growth rates of $[\Sigma_k|B(k)|^2]^{\frac{1}{2}}$ (in units of T^{-1}) *vs.* α for (*a*) the non-reversing-helicity case, $R_m = 10^4$, (*b*) the Bayly–Childress (1988) mapping, $R_m = 10^4$, (*c*) the reversing-helicity case, $R_m = 10^4$, (*d*) the reversing-helicity case, $R_m = 10^3$, and (*e*) the simplified dynamo model, as predicted by equation (9).

(figure 1 *e, f*). This suggests that the mechanism described by the simplified model is the dominant dynamo mechanism for α in the neighbourhood of 0.5. Figure 4 also shows the growth rates obtained for the non-reversing-helicity case (trace *a*). It too exhibits substantial growth near $\alpha = 0.5$ although, interestingly, the growth is somewhat less than in the reversing-helicity case. One would expect the growth rate to be less in the reversing-helicity case since, according to the simplified model, the dynamo-generated field points in the direction opposite to the seed field of the previous flow pulse, which would tend to produce some cancellation.

Diagnostics were installed to allow the display of greyscales of the spatial structure of the various magnetic field components located in individual constant-z planes at specified times. For parameters characteristic of the simplified model, the magnetic field structures shown in figure 5 are typical. In the reversing-helicity case, the strongest magnetic fields tend to congregate along the diagonals of the box in a series of long thin structures. The field lines tend to be directed along the length of these structures. Movies assembled with frames such as those shown in figures 5(*a*) and 5(*b*) show that these structures emerge from the corners at $(x,y) = (0,0)$ and $(2\pi, 2\pi)$ and proceed towards the centre of the box at $(x,y) = (\pi,\pi)$. As the structures approach the centre, they are stretched out along the other diagonal of the box. Additionally, oppositely directed magnetic fields typically 'drop in' from above or below the fixed points located at $(x,y) = (\pi,\pi)$ or $(0,0)$ respectively.

These phenomena are explained by the flow pattern in the limit of infinitesimal pulse width ($\pi/\omega_0 \rightarrow 0$), shown in figure 6(*a*). The diagonals on which the strongest magnetic field structures appear correspond to the boundaries of the convective cells of the flow in this limit, while the motion, stretching, and dropping in of the structures is explained

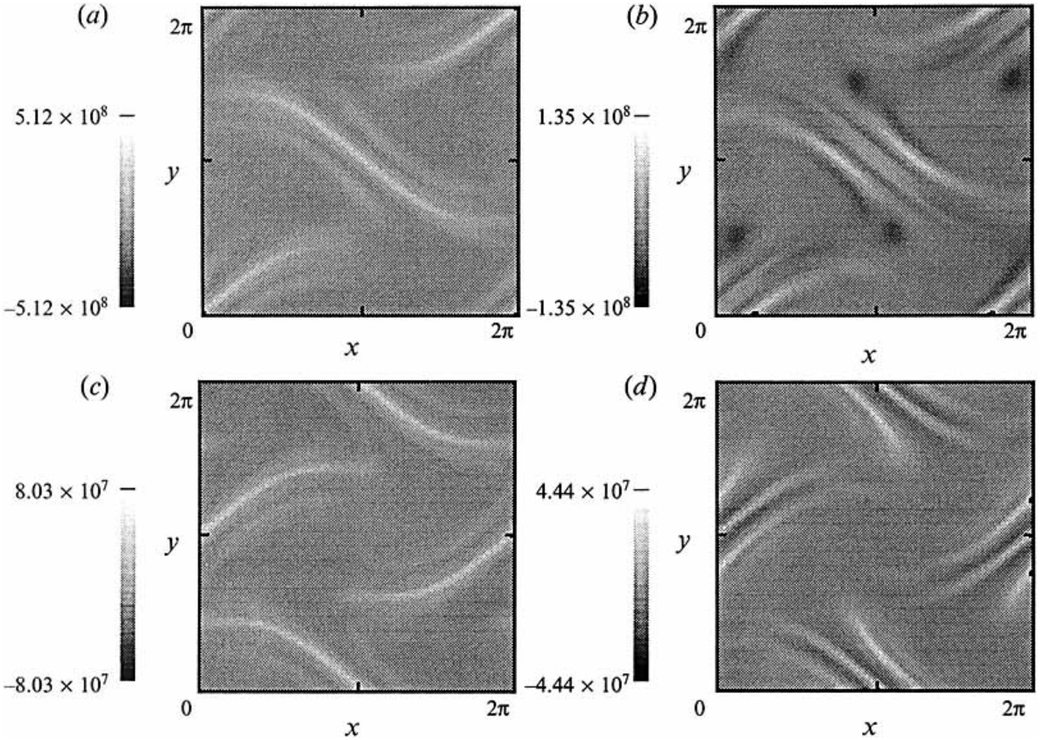

FIGURE 5. Greyscale plots *vs.* x and y at $t = 49.77$ for $R_m = 10^4$ of (a) B_x at $z = 0$ and (b) B_y at $z = \pi/2k_z$ for the reversing-helicity case, and (c) B_x at $z = 0$ and (d) B_y at $z = \pi/2k_z$ for the non-reversing-helicity case.

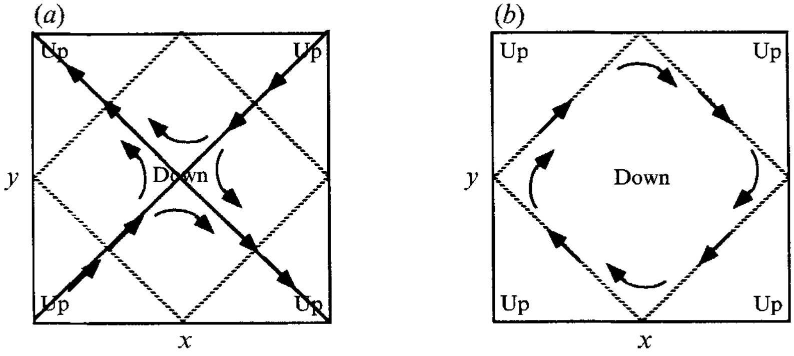

FIGURE 6. Features of (a) the reversing-helicity flow and (b) the non-reversing-helicity flow in the limit of infinitesimally short pulses ($\pi/\omega_0 \rightarrow 0$). The arrows depict the flow in the (x, y)-plane along the convective cell boundaries. The dotted lines outline the boundary between positive (upward) and negative (downward) flow in the $\hat{z}$-direction. Note that the two cases are inherently different. The convective cell boundary coincides with the boundary separating upward and downward flow for the non-reversing-helicity case, and crosses through the centre of the upward and downward flow regions for the reversing helicity case.

by the direction of the flow along these boundaries and the overall $\hat{z}$-component of the flow. The most obvious effect of the finite width of the flow pulses is the observed swaying of the dominant field structures to either side of the infinitesimal-pulse-width convective cell boundary.

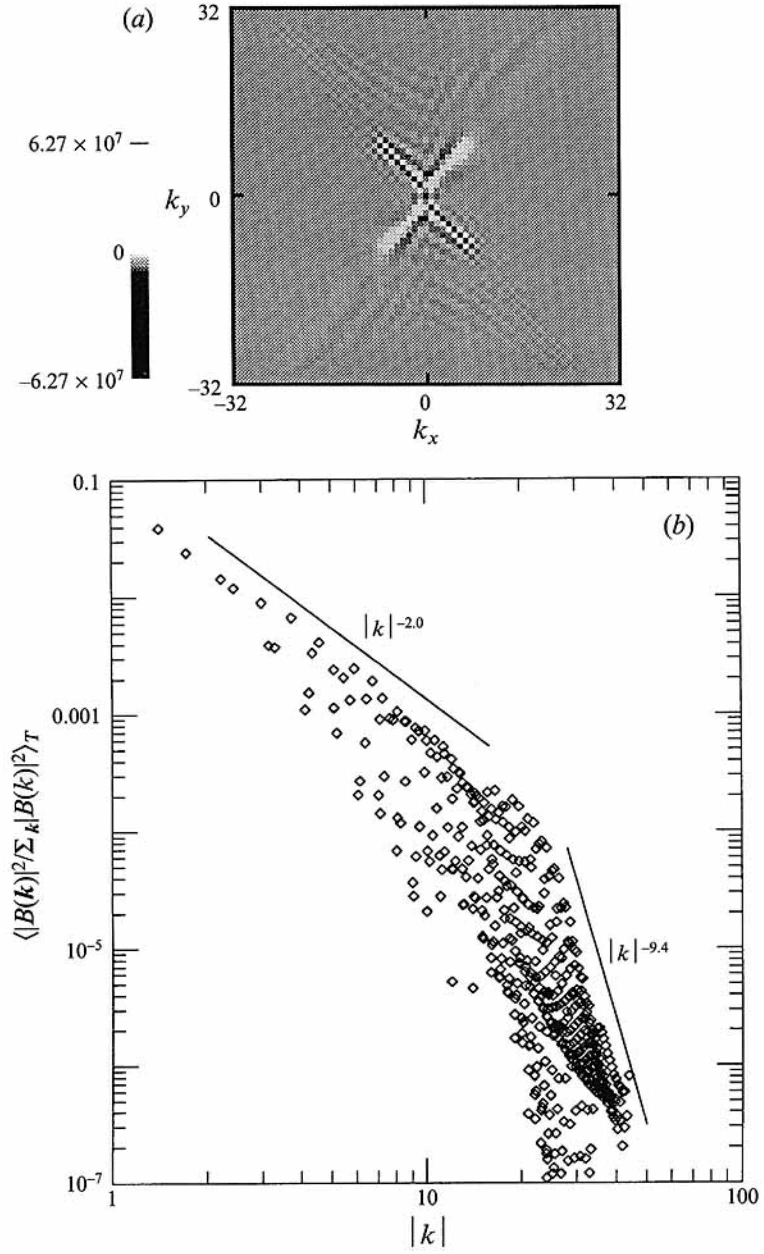

FIGURE 7. (*a*) Greyscale plot of the real part of the Fourier transform of B_x at time $t = 49.77$ for $R_m = 10^4$. The scale has been expanded to show the low-amplitude, high-k modes. The amplitudes of these modes are approximately 1/100th those of the largest low-k modes. (*b*) Plot *vs.* $|k|$ of $|B(k,t)|^2/\Sigma_k|B(k,t)|^2$ averaged over one pulse period: $t = 46.63$ to 49.77. An average over the period $t = 25.00$ to 28.14 produced a nearly identical spectrum.

The non-reversing magnetic field structure, shown in figures 5(*c*) and 5(*d*), exhibits analogous features in the same zero-pulse-width limit (figure 6*b*). Note that this flow is intrinsically different from the reversing helicity flow of figure 6(*a*). Field structures are not observed to drop in for the non-reversing-helicity case, because the main upward and downward convection occurs in the centre of the convective cells, where

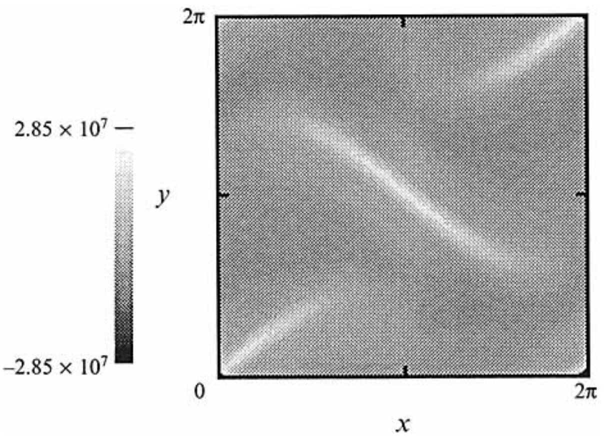

FIGURE 8. Greyscale plots *vs.* x and y at $t = 49.77$ for $R_m = 10^3$ of B_x at $z = 0$ for the reversing-helicity case.

the field is relatively weak, rather than on the convective cell boundary. This may account for the somewhat smaller growth of the non-reversing-helicity case for $\alpha = 0.5$ mentioned earlier.

A comparison of figures 5(*c*) and 5(*d*) with 5(*a*) and 5(*b*) also reveals features consistent with the time histories displayed in figure 3 in the vicinity of $t = 49.77$. B_x in figures 5(*a*) and 5(*c*) is predominantly positive (evidenced by the predominance of the lighter shades of grey), having just been stretched by the $\hat{x}$-directed flow with $\sin^2 \omega_0 t$ time dependence. In contrast, B_y appears with both polarities in figure 5(*b*), as a result of field being dropped in by flow in the z-direction arising from the onset of the $\cos^2 \omega_0 t$ pulse. By and large, only a single polarity for B_y appears in figure 5(*d*), since what little z-directed flow occurs in the strong magnetic field regions serves only to drop in like-directed field, according to the simplified dynamo and infinitesimal-pulse flow models described above.

Figure 7(*a*) shows the Fourier space typical of runs exhibiting the dynamo effect. The relatively solid pattern of the upper-right and lower-left arms of the X-pattern and the checkboard pattern of the remaining arms are consistent with the localization of the dominant magnetic field structures near the diagonals in figure 5(*a*). When viewed as a movie, the angle between the arms of the X in Fourier space expands and contracts, like a butterfly beating its wings, in concert with the rhythm of the pulsed flow. Figure 7(*b*) shows the time-averaged normalized power spectrum. Two regimes are apparent, with the transition occurring at about $|k| = 20$. The gradual fall-off of $\sim |k|^{-2}$ for $|k| < 20$ appears to be associated with the large-amplitude central portion of the X in figure 7(*a*). Additional analysis of this spectrum is pending.

Perhaps the most important feature of the Fourier space is the relative insensitivity of the amplitudes of the modes near $k_x = k_y = 0$ (the long-wavelength modes) to the value of the resistivity. As the resistivity is decreased, the low-wavenumber pattern (i.e. $|k_x|, |k_y| \lesssim 7$ in figure 7*a*) at any given time changes very little. The principal difference among Fourier space plots obtained from runs with different resistivities appears not at low but at high k, where, as might be expected, the arms are observed to extend farther into the high-k regions as the resistivity is decreased. The essential spatial structure (e.g. figure 5*a*) is also correspondingly insensitive to the value of the resistivity. When compared to the higher resistivity run shown in figure 8, the spatial structure in figure 5(*a*) shows better definition, but remains otherwise unchanged.

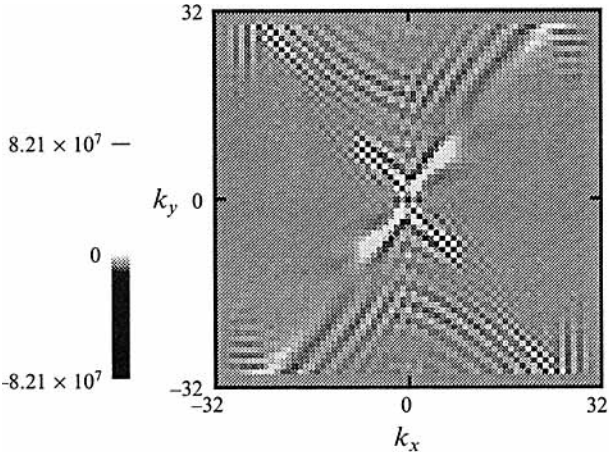

FIGURE 9. Greyscale plot of the real part of the Fourier transform of B_x at time $t = 49.77$ for $\eta = 0$.

We also find that the low-wavenumber pattern does not change at all when the number of Fourier modes is increased from 32 to 64 when $R_m = 10^4$. The primary inference to draw here is that the code, although restricted in its representation of Fourier space, is following the low wavenumbers with reasonable accuracy.

In another test, we tried exciting initially only the highest-k modes kept by our simulation (i.e. those modes near the edge of the Fourier-space box). The magnetic field energy is observed to grow only half as rapidly as normal until the dominant mode is able to establish itself from stray fields. The growth rate then reverted to its original value. The implication is that the growth of the dominant mode is driven by dynamics at long rather than short wavelengths. This, combined with the linearity of the equations in $\boldsymbol{B}$ and the fact that the high-k modes are typically 100 times smaller in amplitude than the low-k modes in typical dynamo runs such as the one depicted in figure 7, suggests that the effect of high-k modes is relatively minor.

One last test we made simply involved setting the resistivity to zero. The simulation in this case is physically invalid, since spatial Fourier modes are excited up to the highest k modes retained which are not properly treated by the simulation. The results are nevertheless of interest. The arms of the X-pattern in Fourier space reach all the way to the edge of the box in this case, and there artificially ‘bounce’ off back towards the centre of the box (figure 9). We find, however, that the amplitudes associated with this ‘reflection’ in Fourier space decay as the reflection propagates away from the edge, and, more importantly, do not seem to affect the primary X-pattern associated with the fastest-growing mode. The growth rates are only slightly different, being higher by approximately 10%. Again, the test suggests that the impact of the short-wavelength modes on the long-wavelength dynamo mechanism is minimal as $R_m \rightarrow \infty$.

5. Conclusions

We have conducted simulations of a physically realizable version of the Bayly–Childress dynamo model which show a number of features strongly suggestive of the presence of a fast dynamo. The results presented here provide compelling but still not definitive evidence for the existence of fast dynamo action within the model. We would like, in particular, to improve our understanding of the effects of short wavelengths on dynamo activity in our simulations as $R_m \to \infty$. The model we employ was designed to produce dynamo activity using a mechanism which relies on a specific coupling of long-wavelength spatial Fourier components of the magnetic field. Within the parameter regime most appropriate to the functioning of this mechanism ($\alpha \sim 0.5$), we obtain growth rates for the largest magnetic Reynolds number we studied ($R_m = 10^4$) which are approximately equal to those expected from the operation of this mechanism. The growth rates obtained also agree well with those found by Bayly & Childress from their mapping model, suggesting that their model is a good representation of our physical model. We can say with confidence that dynamo action exists for fairly large Reynolds numbers ($R_m = 10^4$), since the simulation showed effectively identical behaviour when the number of spatial Fourier modes was doubled. Exponential growth of the magnetic field was observed both for the flow whose helicity reversed between pulses, and for the flow whose helicity did not reverse. The long-wavelength structure was unchanged as R_m was decreased, strongly suggesting, but not proving, that the expected dynamo mechanism would continue to be operative as $R_m \to \infty$. Finally, two non-physical tests, one in which the simulation was initialized with all the energy in the short-wavelength modes, and one with zero resistivity, both suggest that the effect of short-wavelength modes on the long-wavelength dynamo mechanism is not of important consequence as $R_m \to \infty$.

The author has been guided by several useful conversations and communications with B. J. Bayly, S. Childress, A. Gilbert, C. Seyler, P. L. Similon, H. R. Strauss, and A. Thoul. This work was supported by Cornell University and Presidential Young Investigator Award No. ATM-9158072. Computational facilities were provided by the San Diego Supercomputer Center. Graphical and animation software was developed by the National Center for Supercomputing Applications.

REFERENCES

ARNOL'D, V. I. & KORKINA, E. I. 1983 The growth of a magnetic field in a steady incompressible flow. *Vest. Mosk. Un. Ta.* (1), *Math. Mec.* 3, 43–46.

BAYLY, B. J. & CHILDRESS, S. 1987 Fast-dynamo action in unsteady flows and maps in three dimensions. *Phys. Rev. Lett.* **59**, 1573–1576.

BAYLY, B. & CHILDRESS, S. 1988 Construction of fast dynamos using unsteady flows and maps in three dimensions. *Geophys. Astrophys. Fluid Dyn.* **44**, 211–240.

BAYLY, B. & CHILDRESS, S. 1989 Unsteady dynamo effects at large magnetic Reynolds number. *Geophys. Astrophys. Fluid Dyn.* **49**, 23–43.

CHILDRESS, S., COLLET, P., FRISCH, U., GILBERT, A. D., MOFFATT, H. K. & ZASLAVSKY, G. M. 1990 Report on Workshop on Small-Diffusivity Dynamos and Dynamic-Systems held at Observatoire-de-Nice, 25–30 June 1989. *Geophys. Astrophys. Fluid Dyn.* **52**, 263–270.

DOMBRE, T., FRISCH, U., GREENE, J. M., HÉNON, M., MEHR, A. & SOWARD, A. M. 1986 Chaotic streamlines in ABC flows. *J. Fluid Mech.* **167**, 353–391.

FINN, J. M., HANSON, J. D., KAN, I. & OTT, E. 1991 Steady fast dynamo flows. *Phys. Fluids* B **3**, 1250–1269.

FINN, J. M. & OTT, E. 1988 Chaotic flows and fast magnetic dynamos. *Phys. Fluids* **31**, 2992–3011.

GALLOWAY, D. & FRISCH, U. 1986 Dynamo action in a family of flows with chaotic streamlines. *Geophys. Astrophys. Fluid Dyn.* **36**, 58–83.

GALLOWAY, D. J. & PROCTOR, M. R. E. 1992 Numerical-calculations of fast dynamos in smooth velocity-fields with realistic diffusion. *Nature* **356**, 691–693.

GILBERT, A. D. 1991 Fast dynamo action in a steady chaotic flow. *Nature* **350**, 483–485.

GILBERT, A. D. & CHILDRESS, S. 1990 Evidence for fast dynamo action in a chaotic web. *Phys. Rev. Lett.* **65**, 2133–2136.

Otani, N. F. 1988 Computer simulation of fast kinematic dynamos. *EOS Trans. Am. Geophys. Union* **69**, 1366 (abstract).

Roberts, P. H. & Soward, A. M. 1992 Dynamo theory. *Ann. Rev. Fluid Mech.* **24**, 459–512.

Soward, A. M. 1987 Fast dynamo action in a steady flow. *J. Fluid Mech.* **180**, 267–295.

Strauss, H. R. 1986 Resonant fast dynamo. *Phys. Rev. Lett.* **57**, 2231–2233.

Vaĭnshteĭn, S. I. & Zel'dovich, Ya. B. 1972 Origin of magnetic fields in astrophysics. *Usp. Fiz. Nauk.* **106**, 431–457 (*Sov. Phys. Usp.* **15**, 159–172).